Plasmon Enhanced Photocatalysis with Group IV Metal Nitride and TiO_2 Composites: Rhodamine B Dye Degradation Case Study

Dreenan Shea,[a] Victoria White and Mita Dasog[a,]*

[a] *Department of Chemistry, Dalhousie University, 6243 Alumni Crescent, Halifax, NS, B3H4R2, Canada.*

**Corresponding author email: mita.dasog@dal.ca*

Keywords: Plasmonic, metal nitrides, photocatalysis, titanium dioxide, composites

Abstract

Traditional photocatalysis often employs TiO_2 for its affordability and safety, but its large bandgap (>3 eV) limits solar absorption to under 5%. Plasmonic materials serve as sensitizers to expand absorption into the visible and near-IR spectrum while generating localized electromagnetic fields, hot carriers, and heat to boost catalytic efficiency. While noble metals have been extensively studied for visible light absorption, their high cost and poor oxidative stability have spurred interest in alternative plasmonic materials. Transition metal nitrides, such as TiN, ZrN, and HfN, offer strong absorption in the visible and near-IR regions and are cost-effective. In this study, TiN, ZrN, and HfN were combined with traditional P25 TiO_2 to yield composite materials and their photocatalytic activity was evaluated by monitoring rhodamine B dye degradation. Under optimized conditions and 100 mW cm^{-2} illumination, degradation efficiencies of 96, 71, and 99% were observed for TiN/TiO_2, ZrN/TiO_2, and HfN/TiO_2, respectively. Reaction temperature and power density studies allude to reaction efficiency enhancement due to a hot carrier driven process in TiN/TiO_2 and ZrN/TiO_2 systems. In the case of HfN/TiO_2, photothermal contributions are likely to be significant.

Introduction

Plasmon-enhanced photocatalysis converges the fields of nanotechnology, material science, and photochemistry, aiming to improve the efficiency and applicability of photocatalytic processes. It has been explored for degrading organic pollutants and pathogens in water and air,[1,2] hydrogen production through water splitting,[3] conversion of carbon dioxide into value-added hydrocarbons,[4] nitrogen reduction to ammonia,[5] among others.[6] The fundamental principle of plasmon-enhanced photocatalysis is the exploitation of localized surface plasmon resonance (LSPR). When plasmonic nanoparticles (NPs) are exposed to light of specific wavelengths, their conduction electrons oscillate collectively, creating an intense electromagnetic field at the particle surface. This phenomenon, known as LSPR, leads to several beneficial effects that enhance photocatalytic activity as outlined below.

Plasmonic materials often absorb in the visible and near-IR regions of the electromagnetic spectrum thus acting as sensitizers for the photocatalyst and enhance their light absorption capability.[7] The intense electromagnetic fields generated by LSPR can boost the generation of electron-hole pairs necessary for driving photocatalytic reactions.[8] Additionally, the decay of LSPR results in the production of highly energetic "hot" electrons, which can be injected into the conduction band of an adjacent semiconductor photocatalyst, thus increasing the number of charge carriers available for chemical transformations and enhancing charge separation.[9] Plasmonic NPs can also enhance photocatalytic processes through near-field enhancement, where the electromagnetic field around the photocatalyst is significantly increased, leading to higher reaction rates.[7,10] The absorbed light can be converted into heat through non-radiative decay of plasmons. This photothermal effect increases the local temperature around the photocatalyst, which can increase reaction rates according to the Arrhenius equation.[11,12] Plasmonic NPs can scatter the

incident light, extending the optical path length within the photocatalytic material and thus increasing the probability of light absorption.[7] While there are multiple pathways through which photocatalytic efficiency can be enhanced, understanding the intricate mechanisms at play can be challenging.

Plasmonic metals such as Au, Ag, Cu, Al, Ni, Pt, Pd and Ru have been integrated with semiconductors to improve their photocatalytic performance.[13–15] However, the high cost, low abundance, and chemical instability of commonly used metal nanoparticles remain a hurdle and as such interest in the use of alternative plasmonic materials has expanded in the recent years. Refractory materials, like transition metal nitrides (TMNs), have received significant interest due to their tunable optical properties and high thermal and chemical stability.[16,17] Among these TiN is the most explored and has been used to enhance the rates of water splitting,[18–21] CO_2 reduction,[22,23] and organic degradation and transformation reactions.[24–28] The related group IV nitrides, ZrN and HfN are less explored, but few studies exist showing their ability to enhance photocatalytic activity in energy applications.[29–31] Most studies reported to date involving group IV plasmonic nitrides propose an improvement in the photocatalytic activity due to sensitization and hot carrier injection driven pathways. However, studies performed by Zhao *et al*. showed that 25% of the enhancement in hydrogen production with their TiN/TiO_2 catalyst resulted due to photothermal effects.[20] Ru decorated TiN nanotubes have been successfully applied for photothermally driven CO_2 methanation reaction in the gas phase.[28] Given the infancy of the nitride plasmonic materials, the enhancement pathways when utilizing these nanostructures remain poorly understood. But this knowledge informs the design of more robust and selective catalysts for specific reactions.

In this study, a systematic evaluation was performed on TMN/TiO_2 photocatalysts (TMN = TiN, ZrN, and HfN) using rhodamine B (RhB) dye as a model compound. The rate of degradation as function of catalyst loading, weight percent (wt%) of TMN, and dye concentration was studied. The rate of RhB degradation as a function of light intensity and reaction temperatures was investigated to understand the plasmonic enhancement pathway for each TMN on TiO_2.

Results and Discussion

The plasmonic group IV TMNs were synthesized using a solid-state metathesis method reported previously.[32] This yielded crystalline TiN, ZrN, and HfN product with a rock salt structure as determined by the powder X-ray diffraction (XRD) patterns (Figure S1). Transmission electron microscopy (TEM) images showed an average particle size of 22 ± 3, 24 ± 4, and 16 ± 4 nm for TiN, ZrN, and HfN, respectively (Figure S2). The absorbance spectra of TMN aqueous dispersions (Figure S3) showed LSPR maxima at approximately 795, 600, and 550 nm for TiN, ZrN, and HfN, respectively, consistent with previous results.[17] The P25 TiO_2 NPs with an average particle size of 23 ± 4 nm (Figure S2) were commercially purchased. Powder XRD analysis (Figure 1A) showed the TiO_2 NPs to contain both anatase and rutile phase consistent with the literature reports.[33] To obtain the composite material, P25 TiO_2 was combined with predetermined amounts (1, 5, 10, and 20 wt%) of TMN NPs and annealed at 200 °C for 3 hours under argon atmosphere. The aqueous washes from the annealed product were clear indicating that the TMNs were strongly bound to the TiO_2 NPs. This likely results from condensation of surface hydroxyl groups found on both materials.[17]

The powder XRD patterns of the 10 wt% TMN/TiO_2 composites show patterns similar to P25 TiO_2 without discernable nitride reflections (Figure 1A). However, the absorbance spectra of

the 10 wt% TMN/TiO_2 composite material were significantly different from the parent TiO_2 NPs (Figure 1B). The composites showed broader absorbance ranging from near-UV to near-IR with HfN/TiO_2 having the highest absorbance followed by ZrN/TiO_2 and TiN/TiO_2. In contrast, the TiO_2 NPs exhibited strong absorbance only below 425 nm. This is further evident from the photographs of the composite powders which appear blue to greyish color whereas TiO_2 NPs are white (Figure 1B inset).

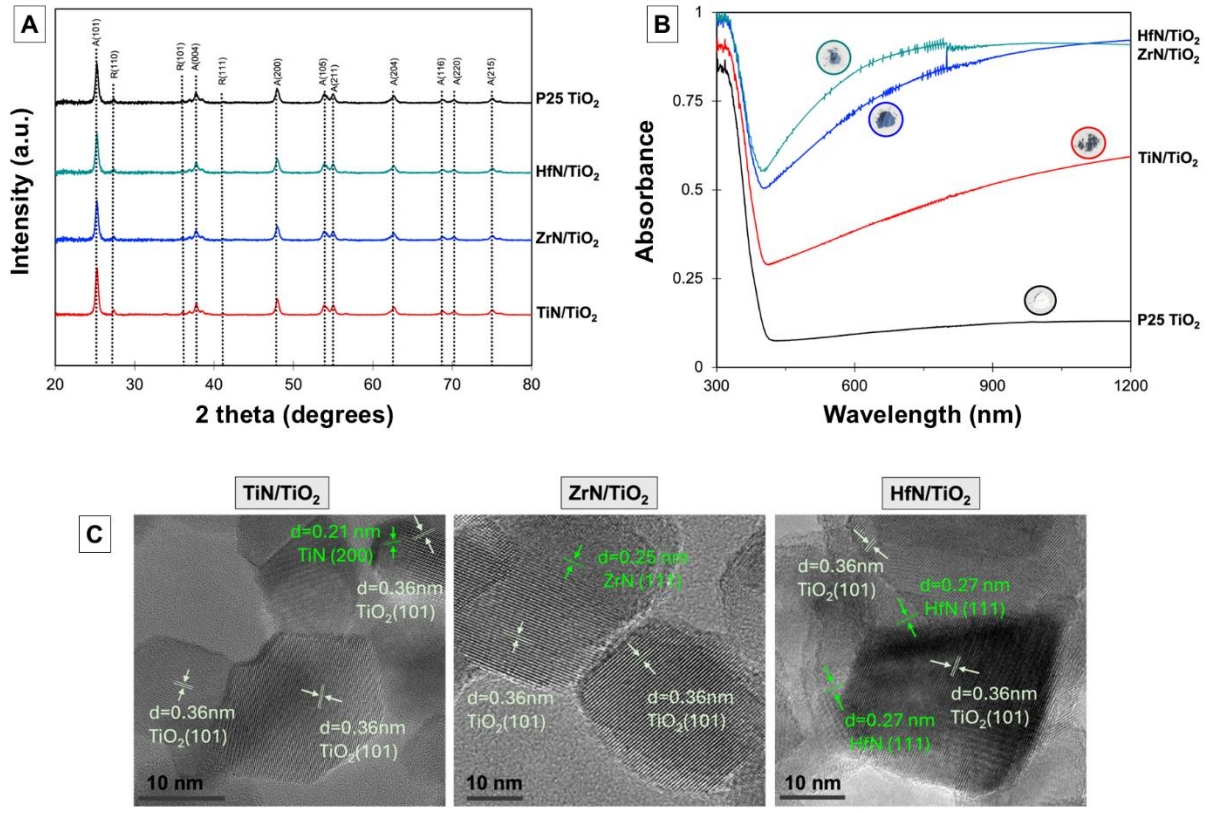

Figure 1. (A) Powder XRD patterns and (B) absorbance spectra of the pure P25 TiO_2 NPs and 10 wt% TMN/TiO_2 composites. (C) High resolution TEM images of the 10 wt% TMN/TiO_2 composites.

The high-resolution TEM images of the composite material showed TMNs adjacent to TiO_2 particles as shown in Figure 1C. The d-spacing for TiN (200), ZrN (111), HfN (111), and TiO_2 (101) planes were determined to be 0.21, 0.25, 0.27, and 0.36 nm, respectively, which is

consistent with previous reports.[34–36] The elemental maps of the P25 TiO_2 and pure TMNs showed the presence of respective transition metals along with N and O (Figure S4). The average O content in TMNs was determined to be 21% (TiN), 20% (ZrN), and 11% (HfN) using energy-dispersive X-ray spectroscopy (EDS) analysis (Table S1), which is due to the surface oxidation of the NPs.[17] Surprisingly, ~5% N impurity was present in the P25 TiO_2 sample which was not indicated by the supplier (Table S1). The optical gap of 3.05 eV as estimated from Tauc plot (Figure S5) which is slightly smaller than the typically reported values of 3.15 – 3.2 eV reported for P25 TiO_2.[37] We hypothesize this is likely due to the presence of N impurities.[38] The elemental maps of the 10 wt% TMN/TiO_2 composites (Figure 2) showed uniform distribution of the N and O. While the Ti metal in TiO_2 and TiN cannot be separated, Zr and Hf metals were found along with TiO_2 indicating that they are likely attached. The relative concentration of each element is summarized in Table S2.

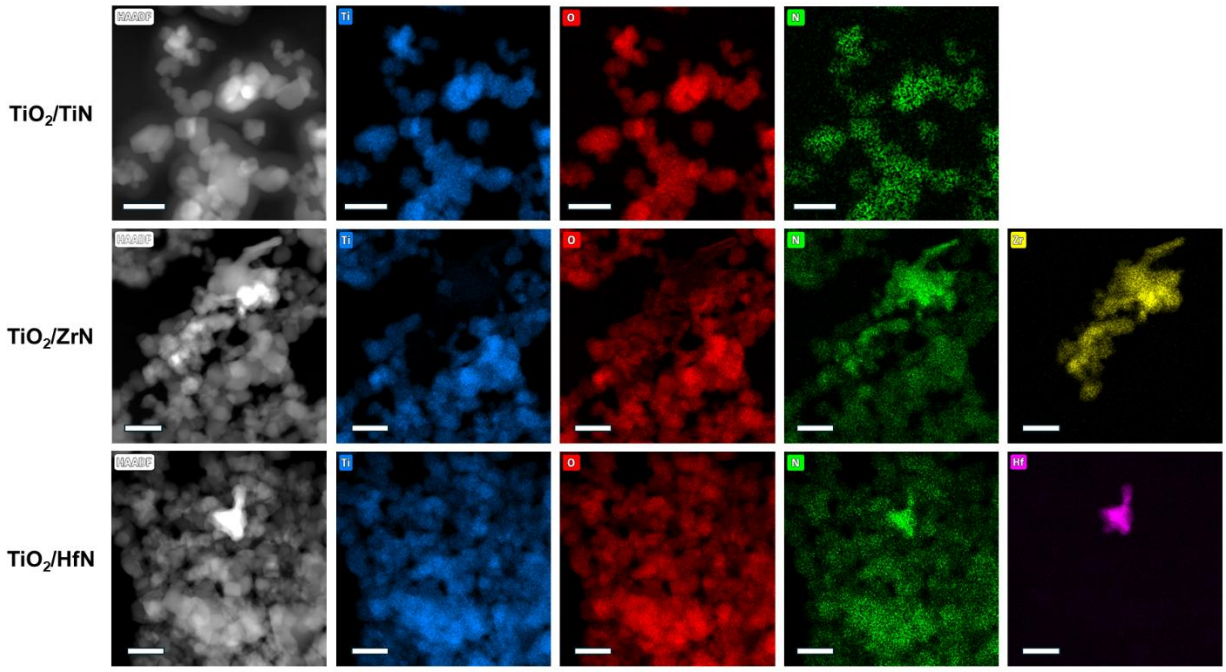

Figure 2. High-angle annular dark-field (HAADF) images and elemental maps of 10wt% TMN/TiO_2 composites where TMN are TiN, ZrN, and HfN. The scale bar in the images correspond to 50 nm.

To understand the photocatalytic performance of TMN/TiO_2 composites, RhB dye was used as a model system as its degradation has been well studied in the literature.[39] Premeasured amount of the photocatalyst was suspended in aqueous solution of the RhB dye and allowed to stir in dark for 30 minutes to establish adsorption-desorption equilibrium (i.e., "light off" region in Figure 3A). After 30 minutes, the reaction was illuminated with a broadband ThorLabs SOLIS LED source (400 – 800 nm) adjusted to a power of 100 mW cm^{-2}. The degradation was monitored by measuring the absorbance maximum of the dye (Figure S6) and comparing it with a calibration curve.[40] In the presence of 10 µM RhB dye and 1 mg mL^{-1} photocatalyst, the P25 TiO_2 NPs by themselves showed 50% degradation after 50 minutes of light exposure (Figure 3A). Given the low absorbance of the TiO_2 NPs in the visible and near-IR range, it is unsurprising that it had the lowest activity. Among the 10 wt% TMN/TiO_2 composites, the HfN/TiO_2 had the highest activity where >99% of dye degradation was observed after 50 minutes of illumination (Figure S7). In the same time frame 10 wt% TiN/TiO_2 and ZrN/TiO_2 showed 95 and 70% degradation, respectively. The TMNs by themselves at similar catalyst loading (i.e., 1 mg/mL) and 10 µM RhB concentration showed 43, 39, and 46% degradation for TiN, ZrN, and HfN, respectively, after 50 minutes and 100 mW cm^{-2} illumination power. The degradation observed with the pure TiO_2 and TMNs are all lower than the composite materials. Control experiments were also performed by simply adding 10 wt% of TMN and TiO_2 (i.e., unannealed samples) to the catalytic mixture. This showed 40, 31, and 43% RhB degradation for TiN, ZrN, and HfN, respectively after 50 minutes of irradiation. This confirms that the formation of a heterojunction and synergistic effects of TiO_2 and TMN together, results in enhanced photocatalytic activity. The kinetics of the dye degradation was analyzed and showed best fit (i.e., linear relationship) to the first-order reaction rate (Figure S8).

As expected, HfN/TiO_2 had the highest rate constant with a k_1 value of 0.117 min^{-1}, followed by TiN/TiO_2 (0.072 min^{-1}), ZrN/TiO_2 (0.032 min^{-1}), and finally TiO_2 (0.005 min^{-1}), which showed the lowest photodegradation.

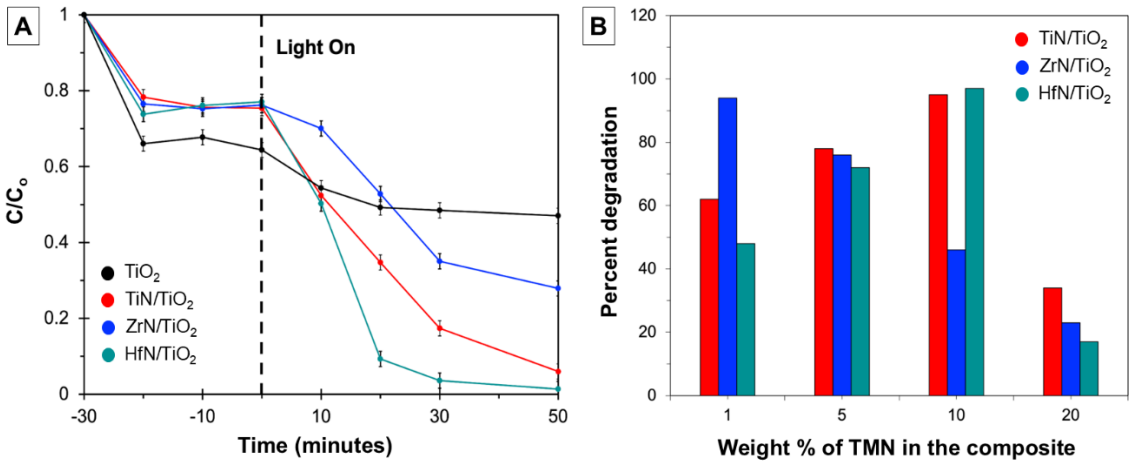

Figure 3. A) Photocatalytic RhB degradation profile in the presence of pure P25 TiO_2 and 10wt% TMN/TiO_2 photocatalysts under 100 mW cm^{-2} illumination. B) The percent degradation of RhB dye over 50 minutes of illumination in the presence of 1 – 20 wt% TMN/TiO_2 photocatalysts.

Since HfN/TiO_2 showed the highest photocatalytic activity among all three TMN/TiO_2 composites, it was used to study the effect of dye concentration and catalyst loading on RhB degradation. As shown in Figure S9, the concentration of RhB impacted the catalytic activity, as near complete degradation (>99%) was observed after 50 minutes when using a 10 μM solution, whereas only 30% degradation was achieved when using a higher dye concentration of 50 μM. The inverse relationship between degradation efficiency and initial RhB dye concentration is likely due to the absorption of the incoming irradiation by the dye.[41] As fewer photons become available for the photocatalyst to absorb, fewer electron-hole pairs are generated, limiting photo-degradation of RhB. Further, an increase in dye concentration generates a scarcity of active sites available,

leading to a decrease in degradation capacity.[42] To understand the dependence of degradation efficiency on the amount of catalyst present in the reaction mixture, trials were run with 10% HfN/TiO_2 loadings ranging from 0.25 – 4 mg mL^{-1}, keeping the solution volume constant at 5 mL. As seen in Figure S10, the degradation efficiency increases with the catalyst concentration reaching a maximum at 1 mg mL^{-1}. After that the activity begins to decrease as more catalyst is added. This trend is commonly observed in photocatalytic studies, as more electron-hole pairs are available with more catalyst present. However, as the catalyst loading increases, the particles can begin to aggregate in solution and scatter the incoming irradiation thus decreasing efficiency.[42]

The effect of TMN amounts in the composite photocatalyst was also investigated, as the plasmonic enhancement capability and pathway can be dependent on its concentration.[1] As shown in Figure 3B, both TiN and HfN had relatively similar trends when the wt% loading was increased from 1 to 20%. At 1 wt% loading, moderate degradation (~50 – 60%) of RhB dye was achieved, which increased to around 70% with a loading at 5 wt%. Over 95% of the RhB dye degradation was achieved at 10% TiN/TiO_2 and HfN/TiO_2 loading making it the optimum composition for TiN and HfN. However, the degradation performance plummeted for both TiN (35%) and HfN (15%) when the loading was further increased to 20 wt% TMN/TiO_2. ZrN/TiO_2 heterostructures exhibited a different behaviour in which highest catalytic activity (i.e., 94% degradation) was observed at 1 wt% loading and the performance decreased with higher ZrN loading.

Plasmonic materials in conjunction with a semiconductor can enhance the photocatalytic performance through multiple pathways which include, increasing light absorption, hot carrier injection and improved charge separation, by increasing reaction temperature, and/or via energy transfer mechanisms.[1–3,43] In the case of TMNs, the dominant catalytic efficiency enhancement pathway proposed to-date involves the transfer of hot-carriers.[31,44,45] Group IV TMNs form an

Ohmic contact with TiO_2 whereas most noble metals create a Schottky junction.[46] Previous studies performed on TiN/TiO_2 systems have proposed such a junction to be beneficial as it allows for the transfer of both the hot electrons and cold electrons from the interband transitions in TiN to TiO_2.[45] Further, the broad absorbance of TMNs allows collection of more photons across the solar spectrum. Similarly, studies performed on HfN/TiO_2 system have proposed that hot electrons can be transferred from HfN to TiO_2 to improve the catalytic activity.[31,47] TMNs are also very well known for their photothermal properties,[16] however, the role of heat in photocatalytic systems involving TMN and semiconductor junctions have not been explored in most studies. In plasmonic photocatalytic reactions facilitated by hot carriers, the rate of chemical reaction is directly proportional to the rate of incoming photons and, consequently, to the power of the light striking the sample.[48] Therefore, a linear relationship is expected between the two. In a photothermal process, the reaction rate follows Arrhenius-type temperature dependence and exhibits a non-linear and specifically exponential relationship with the illumination power.[48] Attempts were made to understand the plasmonic enhancement mechanism in group IV TMN/TiO_2 composites by varying illumination intensity and monitoring the reaction temperature.

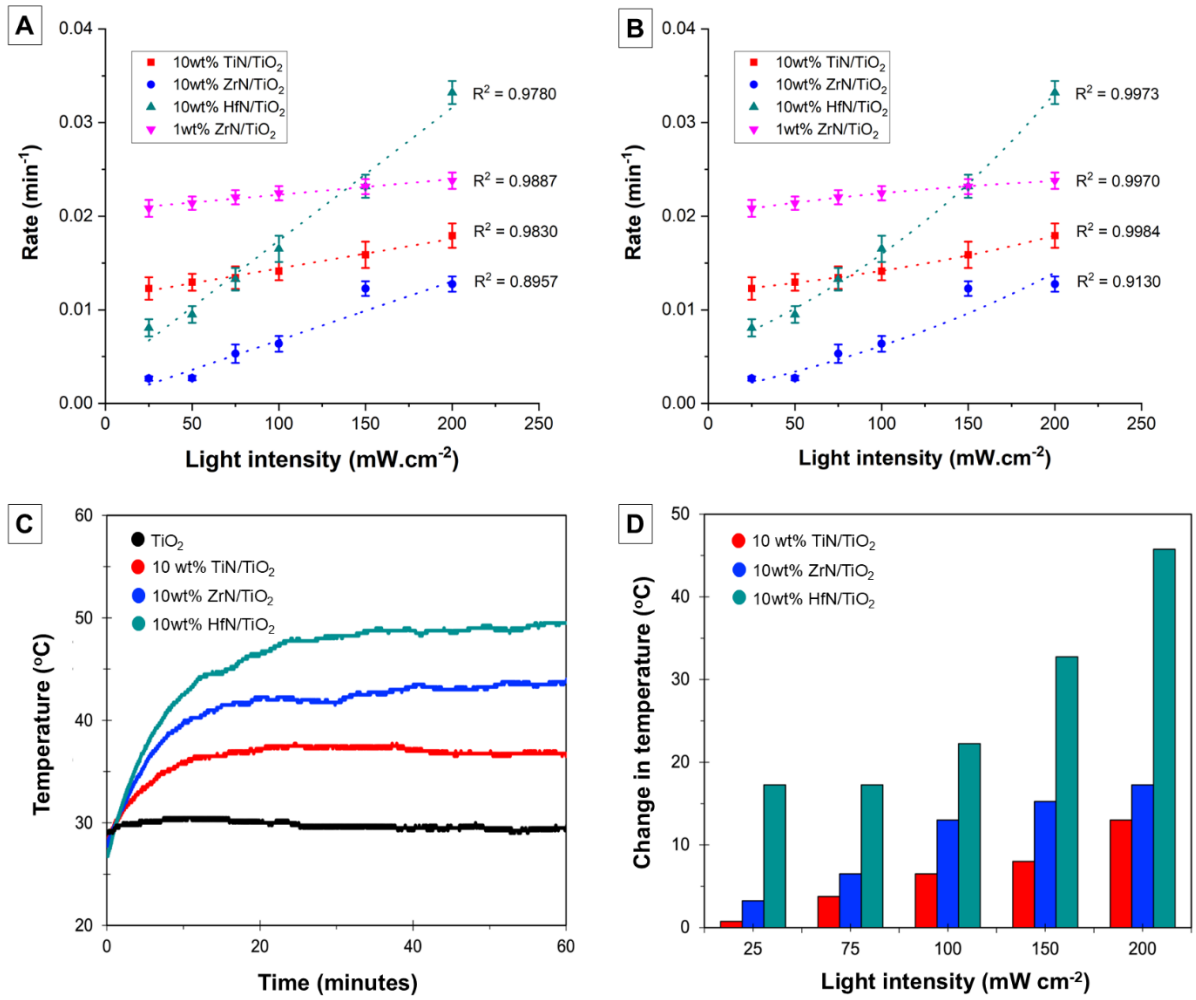

Figure 4. The reaction rate versus illumination power fit to (A) linear and (B) exponential models for RhB degradation in the presence of TMN/TiO_2 photocatalysts. (C) Reaction temperature profile under 100 mW cm^{-2} illumination and (D) maximum reaction temperature achieved at various illumination intensities when using 10wt% TMN/TiO_2 photocatalysts.

Based on the absorbance data, all three TMN/TiO_2 composites exhibited higher light absorption in the visible and near-IR region compared to the P25 TiO_2 (Figure 1B). This sensitization leads to higher concentration of excited electrons that can drive chemical process. The degradation rate of RhB dye was monitored using TMN/TiO_2 photocatalysts under varying incident light power. Data were fit to both linear (Figure 4A) and exponential (Figure 4B) models. The 10 wt% TiN/TiO_2 composite exhibited a good linear fit between the reaction rate and incident

power and an even better exponential fit based on the R^2 value. The 10 wt% HfN/TiO_2 composite showed a better exponential fit. However, the 10 wt% ZrN/TiO_2 samples demonstrated poor correlation with both linear and exponential models in relating reaction rate to illumination power. The reaction temperature was monitored during photocatalysis (Figure 4C). All TMN-containing photocatalysts showed a greater temperature increase compared to the pure P25 TiO_2 catalyst, which exhibited minimal temperature change (<2 °C). Notably, although the TiN/TiO_2 system had the highest R^2 value for the exponential fit indicating a photothermally driven process, it displayed the least temperature rise across all illumination intensities (Figure 4D). This suggests that the enhanced photocatalytic activity in TiN/TiO_2 is likely driven by the transfer of hot carriers rather than photothermal effects. The limited range of light intensities used in this study restricts the ability to clearly distinguish between photothermal and photochemical contributions as observed previously.[48] In contrast, the HfN/TiO_2 composite exhibited the highest temperature increase under all illumination powers (Figure 4D) and a stronger exponential relationship between reaction rate and incident light intensity. This indicates that the photothermal effect likely plays an important role in the photocatalytic process involving HfN/TiO_2. Previous calculations have shown that the excited electrons in HfN NPs thermalize extremely quickly (in 250 femtoseconds) which likely does not allow them to be harvested efficiently by TiO_2.[49] The RhB dye solution was heated to 70 °C to mimic the bulk temperature achieved under 200 mW cm^{-2} illumination with the HfN/TiO_2 system, however, only ~30% degradation was achieved. This suggests that the bulk reaction temperature is not reflective of the photocatalyst surface temperature where the dye is adsorbed, or it is both the hot carrier transfer and heat that contribute towards the RhB degradation in the HfN/TiO_2 system.[50]

The 10wt% ZrN/TiO_2 had a poor linear and exponential fit, therefore, to better understand the system, the best performing composition (i.e., 1wt% ZrN/TiO_2) was analyzed (Figure 4A and B). The 1wt% ZrN catalyst showed similar behavior to the 10wt% TiN suggesting similar enhancement pathways. In systems containing Au and Ag nanostructures, it has been shown that electrons injected into TiO_2 from one plasmonic structure can be transfer into adjacent plasmonic particle at higher loadings leading them to recombine with holes.[51,52] This can lead to a decrease in photocatalytic activity as observed in the 10wt% ZrN/TiO_2 system.[53] The temperature increase in this system was greater than TiN but remained significantly below HfN based photocatalysts especially at higher illumination power (Figure 4D). Based on the reaction temperature changes, it is likely that the photocatalytic efficiency enhancement observed in the TiN and ZrN containing composites is predominantly driven by efficient hot-carrier transfer.

Conclusions

Group IV TMN/TiO_2 composite photocatalysts were synthesized using a simple, low-temperature annealing method. The RhB dye was used as model compound to understand the effect of TMNs on the photocatalytic behaviour of TiO_2. All the TMNs improved the light absorption capability of the parent P25 TiO_2 with HfN and ZrN being much higher than the TiN. Lower loading of ZrN (1 wt%) was sufficient to achieve >99% dye degradation in 50 minutes whereas higher loadings (10 wt%) was required for HfN and TiN. The 10wt% HfN/TiO_2 showed significant increase in the reaction temperature when suspended in water and a good exponential relationship between reaction rate and illumination power, indicating that the degradation is likely thermally driven. While the 1wt% ZrN/TiO_2 and 10wt% TiN/TiO_2 showed a good linear and exponential relationship between the reaction and illumination power, based on the temperature changes

observed, the catalytic process is likely dominated by the electron injection from plasmonic material into the TiO_2 NPs and improved carrier separation.

Experimental Section

Materials. Titanium dioxide (TiO_2, 99.9%, 18 nm), zirconium dioxide (ZrO_2, 99.95%, 20 nm), and hafnium dioxide (HfO_2, 99.99%, 61-80 nm) and magnesium nitride (Mg_3N_2, 99% purity -325 mesh) were purchased from U.S. Research Nanomaterials Inc. Hydrochloric acid (HCl) was purchased from Anachemica (12 M, 37%) and sodium hydroxide (NaOH) from Alfa Aesar (98% purity). Titanium dioxide (TiO_2, P25, 99.5%, 21 nm) and Rhodamine B (95%) were both purchased from Sigma Aldrich. Water (resistivity = 18.2 MΩ.cm) from Sartorius Arium Pro Ultrapure Water System was used for Rhodamine B stock solutions.

Synthesis of Group IV Plasmonic Metal Nitrides. TMN (M = Ti, Zr, or Hf)) NPs were synthesized using a previously reported solid-state reaction.[32] Briefly, metal oxide nanopowder (TiO_2, ZrO_2 or HfO_2) was ground together with Mg_3N_2 using a mortar and pestle in a N_2 filled glovebox in 1:4 (metal oxide:Mg_3N_2) molar ratio. The powder mixture was transferred to a ceramic combustion boat which was placed in a tube furnace and heated to 1000 °C at a ramp rate of 10 °C/min and held at that temperature for 12 h under flowing argon gas. After cooling the reaction mixture to room temperature, the powder was transferred to a beaker and reacted with 1.0 M HCl (25 mL) for 1 h to remove MgO by-product and any unreacted Mg_3N_2. The solution was then centrifuged (15 min at 3300 rpm) and the colorless supernatant was discarded. The precipitate was redispersed in DI-water and centrifuged again (15 min at 3300 rpm), and the brightly coloured supernatant was collected. This step was repeated, and the supernatant was combined with the one from the

previous centrifugation step. This combined solution contains dispersible TMN NPs, and the precipitate is typically composed of larger TMN aggregates which was discarded. Powders used for the synthesis of photocatalyst composites were collected by adjusting the pH of colloidal suspensions to ~5 by adding 1.0 M NaOH solution. Previously, this has been determined to be point of zero charge and results in precipitation of the NPs which were collected via centrifugation (15 min at 3300 rpm) and dried in an oven overnight at 100°C.[17]

Synthesis of TMN/TiO_2 composites. A TMN stock solution of TiN, ZrN or HfN was first made by dispersing 20 mg of the nitride NP powder in 100 mL of ultrapure water. For 10% TMN/TiO_2 hybrids, 10 mL of TMN stock solution was added to a vial with 20 mg of P25 TiO_2. After sonicating for 5 minutes, the solvent was evaporated in an oven at 100°C overnight. The resulting powders were then collected and annealed at 200°C for 3 hours under argon atmosphere. To synthesize 1, 5, and 20% TMN/TiO_2 hybrids the procedure outlined above was used but 200, 40 and 10 mg of P25 TiO_2 was added, respectively.

Material characterization techniques. Powder X-ray diffraction patterns were collected using a Rigaku Ultima IV X-ray diffractometer with CuKα radiation (λ = 1.54 Å). The powder samples were placed on to a zero-background silicon (Si) wafer and the spectra were collected at angles between 20 and 80° at a rate of 3 counts/s. Absorbance spectra were collected using an Agilent CARY 5000 UV-Vis-NIR spectrometer. NP suspensions were placed in a quartz cuvette and DI-water was used as the blank. Absorbance spectra were scanned at a medium rate between 200 and 1200 nm. For powder samples, an external diffuse reflectance accessory attachment was used on Agilent CARY 5000 with a 150 mm integration sphere. The instrument was used in double beam

mode using reduced slit height and was standard calibrated using a zero/baseline correction. Absorbance values were calculated from reflectance data using the following equation:

$$A = (1 - R)\ x\ 100\%$$

where *A* and *R* are absorbance and the measured reflectance, respectively. There is no transmission through the interfaces so it can be disregarded. High-resolution transmission electron microscopy images were collected using a Thermo Fisher Scientific Talos 200X microscope with an accelerating voltage of 200 kV. HAADF was performed with a spot size less than 1 nm, and a convergence semi-angle of 10.5 mrad. Energy dispersive X-ray mapping was also performed on Talos 200X using SDD Super-X detectors. Image software was used for particle size and lattice spacing analysis.[54]

Photocatalytic Rhodamine B degradation setup. In a typical degradation experiment, 5 mg of the photocatalyst was suspended in 5.0 mL of a 10 μM aqueous RhB dye solution in a glass flask. The mixture was stirred for 30 minutes in the dark to ensure adequate adsorption-desorption equilibration of the dye on the surface of the catalyst. The reaction flask was then illuminated with a high-power SOLIS-3C Thor Labs LED (day light white spectrum) with a power density of 100 mW/cm^2. To understand the effect of light intensity of reaction rates, the illumination intensity was varied between 25 and 200 mW/cm^2. The illumination power density was calibrated using a silicon photodiode (ThorLabs). To monitor the reaction progress, the dye solution was centrifuged to remove the catalyst, and subsequently analyzed using absorbance spectroscopy and the data was collected every 10 minutes. To trace the degradation of the dye, the intensity of the absorbance maxima for RhB (523 – 557 nm) was quantified and compared to a calibration curve to calculate the concentration of dye. Each type of reaction was performed at least three times. To examine the

effect of catalyst loading, the amount of 10wt% HfN/TiO_2 composite was varied between 1.25 – 20 mg and suspended in 5.0 mL of a 10 μM aqueous rhodamine B dye solution in a glass flask. The reaction was performed according to the procedure outlined above. To study the effect of RhB dye amount, the concentration was varied between 10 – 50 μM and 5 mg of the 10wt% HfN/TiO_2 photocatalyst was used.

Temperature measurement setup. The reaction temperatures were measured using a K-type thermocouple which was inserted in the reaction flask through a septum to prevent boiling and subsequent solvent evaporation. The thermocouple was connected to an Arduino electronic platform and data was collected and logged via an open-source Arduino software.

Conflicts of interest

There are no conflicts to declare.

Electronic Supplementary Information

See supplementary materials for Figures S1 –S10 and tables S1 and S2.

Acknowledgements

The authors acknowledge funding from Canada Foundation for Innovation (CFI), Research Nova Scotia (RNS), Natural Sciences and Engineering Research Council of Canada (NSERC), and Killam Trusts. The Canadian Centre for Electron Microscopy and Dr. Carmen Andrei are thanked for TEM, HAADF and elemental mapping experiments. DS thanks the Sumner Foundation for graduate fellowships and VW thanks funding from NSERC USRA program.

References

(1) Nazir, A.; Huo, P.; Wang, H.; Weiqiang, Z.; Wan, Y. A Review on Plasmonic-Based Heterojunction Photocatalysts for Degradation of Organic Pollutants in Wastewater. *J. Mater. Sci.* **2023**, *58* (15), 6474–6515. https://doi.org/10.1007/s10853-023-08391-w.

(2) Wang, D.; Pillai, S. C.; Ho, S.-H.; Zeng, J.; Li, Y.; Dionysiou, D. D. Plasmonic-Based Nanomaterials for Environmental Remediation. *Appl. Catal. B Environ.* **2018**, *237*, 721–741. https://doi.org/10.1016/j.apcatb.2018.05.094.

(3) Ly, N. H.; Vasseghian, Y.; Joo, S.-W. Plasmonic Photocatalysts for Enhanced Solar Hydrogen Production: A Comprehensive Review. *Fuel* **2023**, *344*, 128087. https://doi.org/10.1016/j.fuel.2023.128087.

(4) Li, C.; Wang, J.; Tong, L.; Wang, Y.; Zhang, P.; Zhu, M.; Dong, H. Recent Progress and Challenges of Photocatalytic CO_2 Conversion into Value-Added Multi-Carbon Products. *Coord. Chem. Rev.* **2024**, *502*, 215623. https://doi.org/10.1016/j.ccr.2023.215623.

(5) Ziegenbalg, D.; Zander, J.; Marschall, R. Photocatalytic Nitrogen Reduction: Challenging Materials with Reaction Engineering. *ChemPhotoChem* **2021**, *5* (9), 792–807. https://doi.org/10.1002/cptc.202100084.

(6) Gellé, A.; Jin, T.; de la Garza, L.; Price, G. D.; Besteiro, L. V.; Moores, A. Applications of Plasmon-Enhanced Nanocatalysis to Organic Transformations. *Chem. Rev.* **2020**, *120* (2), 986–1041. https://doi.org/10.1021/acs.chemrev.9b00187.

(7) Wang, T.; Wang, H.-J.; Lin, J.-S.; Yang, J.-L.; Zhang, F.-L.; Lin, X.-M.; Zhang, Y.-J.; Jin, S.; Li, J.-F. Plasmonic Photocatalysis: Mechanism, Applications and Perspectives. *Chin. J. Struct. Chem.* **2023**, *42* (9), 100066. https://doi.org/10.1016/j.cjsc.2023.100066.

(8) Zhan, C.; Yi, J.; Hu, S.; Zhang, X.-G.; Wu, D.-Y.; Tian, Z.-Q. Plasmon-Mediated Chemical Reactions. *Nat. Rev. Methods Primer* **2023**, *3* (1), 1–21. https://doi.org/10.1038/s43586-023-00195-1.

(9) Christopher, P.; Moskovits, M. Hot Charge Carrier Transmission from Plasmonic Nanostructures. *Annu. Rev. Phys. Chem.* **2017**, *68* (1), 379–398. https://doi.org/10.1146/annurev-physchem-052516-044948.

(10) Zhang, Z. Editorial for Special Issue "Plasmon Assisted Near-Field Manipulation and Photocatalysis." *Nanomaterials* **2023**, *13* (8), 1427. https://doi.org/10.3390/nano13081427.

(11) Song, C.; Wang, Z.; Yin, Z.; Xiao, D.; Ma, D. Principles and Applications of Photothermal Catalysis. *Chem Catal.* **2022**, *2* (1), 52–83. https://doi.org/10.1016/j.checat.2021.10.005.

(12) Mascaretti, L.; Naldoni, A. Hot Electron and Thermal Effects in Plasmonic Photocatalysis. *J. Appl. Phys.* **2020**, *128* (4). https://doi.org/10.1063/5.0013945.

(13) Liu, X.; Huang, B.; Li, J.; Li, B.; Lou, Z. Full-Spectrum Plasmonic Semiconductors for Photocatalysis. *Mater. Horiz.* **2024**, *11* (22), 5470–5498. https://doi.org/10.1039/D4MH00515E.

(14) Sayed, M.; Yu, J.; Liu, G.; Jaroniec, M. Non-Noble Plasmonic Metal-Based Photocatalysts. *Chem. Rev.* **2022**, *122* (11), 10484–10537. https://doi.org/10.1021/acs.chemrev.1c00473.

(15) Abouelela, M. M.; Kawamura, G.; Matsuda, A. A Review on Plasmonic Nanoparticle-Semiconductor Photocatalysts for Water Splitting. *J. Clean. Prod.* **2021**, *294*, 126200. https://doi.org/10.1016/j.jclepro.2021.126200.

(16) Dasog, M. Transition Metal Nitrides Are Heating Up the Field of Plasmonics. *Chem. Mater.* **2022**. https://doi.org/10.1021/acs.chemmater.2c00305.

(17) Shea, D.; Karaballi, R. A.; Jee, S.; Dasog, M. Stability and Surface Functionalization of Plasmonic Group 4 Transition Metal Nitrides. *ChemNanoMat* **2024**, *10* (9), e202400236. https://doi.org/10.1002/cnma.202400236.
(18) Naldoni, A.; Guler, U.; Wang, Z.; Marelli, M.; Malara, F.; Meng, X.; Besteiro, L. V.; Govorov, A. O.; Kildishev, A. V.; Boltasseva, A.; Shalaev, V. M. Solar-Energy Harvesting: Broadband Hot-Electron Collection for Solar Water Splitting with Plasmonic Titanium Nitride (Advanced Optical Materials 15/2017). *Adv. Opt. Mater.* **2017**, *5* (15). https://doi.org/10.1002/adom.201770079.
(19) Yu, X.; Zhao, Z.; Sun, D.; Ren, N.; Ding, L.; Yang, R.; Ji, Y.; Li, L.; Liu, H. TiO2/TiN Core/Shell Nanobelts for Efficient Solar Hydrogen Generation. *Chem. Comm.* **2018**, *54* (47), 6056–6059. https://doi.org/10.1039/C8CC02651C.
(20) Zhao, W.-Q.; Liao, Y.-X.; Chen, Y.-T.; Ma, L.; Yu, Z.-Y.; Ding, S.-J.; Qin, P.-L.; Chen, X.-B.; Wang, Q.-Q. TiN/Anatase/Rutile Phase Junction Obtained by *in-Situ* Thermal Transformation for Efficient Photothermal-Assisted Photocatalytic Hydrogen Generation. *J. Colloid Interface Sci.* **2024**, *669*, 383–392. https://doi.org/10.1016/j.jcis.2024.04.223.
(21) He, X.; Liu, Q.; Xu, D.; Wang, L.; Tang, H. Plasmonic TiN Nanobelts Assisted Broad Spectrum Photocatalytic H_2 Generation. *J. Mater. Sci. Technol.* **2022**, *116*, 1–10. https://doi.org/10.1016/j.jmst.2021.10.033.
(22) Nguyen, N. T.; Yan, T.; Wang, L.; Loh, J. Y. Y.; Duchesne, P. N.; Mao, C.; Li, P.-C.; Ali, F. M.; Xia, M.; Ghoussoub, M.; Kherani, N. P.; Lu, Z.-H.; Ozin, G. A. Plasmonic Titanium Nitride Facilitates Indium Oxide CO_2 Photocatalysis. *Small* **2020**, *16* (49), 2005754. https://doi.org/10.1002/smll.202005754.
(23) Nguyen, N. T.; Xia, M.; Duchesne, P. N.; Wang, L.; Mao, C.; Ali, F. M.; Yan, T.; Li, P.; Lu, Z.-H.; Ozin, G. A. Enhanced CO_2 Photocatalysis by Indium Oxide Hydroxide Supported on TiN@TiO2 Nanotubes. *Nano Lett.* **2021**, *21* (3), 1311–1319. https://doi.org/10.1021/acs.nanolett.0c04008.
(24) Tsai, C.-G.; Tseng, W. J. Preparation of TiN–TiO_2 Composite Nanoparticles for Organic Dye Adsorption and Photocatalysis. *Ceram. Int.* **2020**, *46* (10, Part A), 14529–14535. https://doi.org/10.1016/j.ceramint.2020.02.252.
(25) Beierle, A.; Gieri, P.; Pan, H.; Heagy, M. D.; Manjavacas, A.; Chowdhury, S. Titanium Nitride Nanoparticles for the Efficient Photocatalysis of Bicarbonate into Formate. *Sol. Energy Mater. Sol. Cells* **2019**, *200*, 109967. https://doi.org/10.1016/j.solmat.2019.109967.
(26) Shi, H.; Yao, X.; Lu, S.; Zuo, Y.; Zheng, T.; Jia, L. Photocatalytically Active Semiconductor Cu_3P Unites with Flocculent TiN for Efficient Removal of Sulfamethoxazole. *Catalysts* **2023**, *13* (2), 291. https://doi.org/10.3390/catal13020291.
(27) Fan, X.; Wang, F.; Li, M.; Meharban, F.; Li, Y.; Cui, Y.; Li, X.; Xu, J.; Xiao, Q.; Luo, W. Visible Light Excitation on CuPd/TiN with Enhanced Chemisorption for Catalyzing Heck Reaction. *Chin. Chem. Lett.* **2025**, *36* (1), 110299. https://doi.org/10.1016/j.cclet.2024.110299.
(28) Mateo, D.; Navarro, J. C.; Khan, I. S.; Ruiz-Martinez, J.; Gascon, J. Plasmonic Titanium Nitride Tubes Decorated with Ru Nanoparticles as Photo-Thermal Catalyst for CO_2 Methanation. *Molecules* **2022**, *27* (9), 2701. https://doi.org/10.3390/molecules27092701.
(29) Baturina, O. A.; Epshteyn, A.; Leff, A. C.; Purdy, A. P.; Brintlinger, T.; Simpkins, B. S.; Santiago, E. Y.; Govorov, A. O. Photoelectrochemical Methanol Oxidation Under Visible and UV Excitation of TiO_2-Supported TiN and ZrN Plasmonic Nanoparticles. *J. Electrochem. Soc.* **2021**, *168* (1), 016503. https://doi.org/10.1149/1945-7111/abd605.

(30) Liu, Y.; Zhang, X.; Lu, L.; Ye, J.; Wang, J.; Li, X.; Bai, X.; Wang, W. Nanoplasmonic Zirconium Nitride Photocatalyst for Direct Overall Water Splitting. *Chin. Chem. Lett.* **2022**, *33* (3), 1271–1274. https://doi.org/10.1016/j.cclet.2021.07.054.
(31) Zeng, S.; Muneshwar, T.; Riddell, S.; Manuel, A. P.; Vahidzadeh, E.; Kisslinger, R.; Kumar, P.; Alam, K. M. M.; Kobryn, A. E.; Gusarov, S.; Cadien, K. C.; Shankar, K. TiO_2-HfN Radial Nano-Heterojunction: A Hot Carrier Photoanode for Sunlight-Driven Water-Splitting. *Catalysts* **2021**, *11* (11), 1374. https://doi.org/10.3390/catal11111374.
(32) Karaballi, R. A.; Humagain, G.; Fleischman, B. R. A.; Dasog, M. Synthesis of Plasmonic Group-4 Nitride Nanocrystals by Solid-State Metathesis. *Angew. Chem. Int. Ed.* **2019**, *58* (10), 3147–3150. https://doi.org/10.1002/anie.201813134.
(33) Ohtani, B.; Prieto-Mahaney, O. O.; Li, D.; Abe, R. What Is Degussa (Evonik) P25? Crystalline Composition Analysis, Reconstruction from Isolated Pure Particles and Photocatalytic Activity Test. *J. Photochem. Photobiol. Chem.* **2010**, *216* (2), 179–182. https://doi.org/10.1016/j.jphotochem.2010.07.024.
(34) Hu, C.; Zhang, X.; Gu, Z.; Huang, H.; Zhang, S.; Fan, X.; Zhang, W.; Wei, Q.; Zheng, W. Negative Effect of Vacancies on Cubic Symmetry, Hardness and Conductivity in Hafnium Nitride Films. *Scr. Mater.* **2015**, *108*, 141–146. https://doi.org/10.1016/j.scriptamat.2015.07.002.
(35) Dong, K. F.; Deng, J. Y.; Peng, Y. G.; Ju, G.; Chow, G. M.; Chen, J. S. Columnar Structured FePt Films Epitaxially Grown on Large Lattice Mismatched Intermediate Layer. *Sci. Rep.* **2016**, *6* (1), 34637. https://doi.org/10.1038/srep34637.
(36) Thi Le, T.-L.; Nguyen, L. T.; Nguyen, H.-H.; Nghia, N. V.; Vuong, N. M.; Hieu, H. N.; Thang, N. V.; Le, V. T.; Nguyen, V. H.; Lin, P.-C.; Yadav, A.; Madarevic, I.; Janssens, E.; Bui, H. V.; Ngoc, L. L. T. Titanium Nitride Nanodonuts Synthesized from Natural Ilmenite Ore as a Novel and Efficient Thermoplasmonic Material. *Nanomaterials* **2021**, *11* (1), 76. https://doi.org/10.3390/nano11010076.
(37) Hurum, D. C.; Agrios, A. G.; Gray, K. A.; Rajh, T.; Thurnauer, M. C. Explaining the Enhanced Photocatalytic Activity of Degussa P25 Mixed-Phase TiO_2 Using EPR. *J. Phys. Chem. B* **2003**, *107* (19), 4545–4549. https://doi.org/10.1021/jp0273934.
(38) Asahi, R.; Morikawa, T.; Irie, H.; Ohwaki, T. Nitrogen-Doped Titanium Dioxide as Visible-Light-Sensitive Photocatalyst: Designs, Developments, and Prospects. *Chem. Rev.* **2014**, *114* (19), 9824–9852. https://doi.org/10.1021/cr5000738.
(39) Mohod, A. V.; Momotko, M.; Shah, N. S.; Marchel, M.; Imran, M.; Kong, L.; Boczkaj, G. Degradation of Rhodamine Dyes by Advanced Oxidation Processes (AOPs) – Focus on Cavitation and Photocatalysis - A Critical Review. *Water Resour. Ind.* **2023**, *30*, 100220. https://doi.org/10.1016/j.wri.2023.100220.
(40) Chen, X.; Xue, Z.; Yao, Y.; Wang, W.; Zhu, F.; Hong, C. Oxidation Degradation of Rhodamine B in Aqueous by UV/S2O8 2− Treatment System. *Int. J. Photoenergy* **2012**, *2012* (1), 754691. https://doi.org/10.1155/2012/754691.
(41) Kumar, V.; Singh, M.; Behera, K.; Pandey, S. Ionic Liquid Induced Removal of Rhodamine B from Water. *J. Mol. Liq.* **2020**, *319*, 114195. https://doi.org/10.1016/j.molliq.2020.114195.
(42) Bajpai, J. S.; Barai, D. P.; Bhanvase, B. A.; Pawade, V. B. Sonochemical Preparation and Characterization of Sm-Doped GO/$KSrPO_4$ Nanocomposite Photocatalyst for Degradation of Methylene Blue Dye. *Water Environ. Res.* **2022**, *94* (1), e1682. https://doi.org/10.1002/wer.1682.

(43) Kumar, A.; Choudhary, P.; Kumar, A.; Camargo, P. H. C.; Krishnan, V. Recent Advances in Plasmonic Photocatalysis Based on TiO_2 and Noble Metal Nanoparticles for Energy Conversion, Environmental Remediation, and Organic Synthesis. *Small* **2022**, *18* (1), 2101638. https://doi.org/10.1002/smll.202101638.
(44) Liu, T.; Wang, Q.; Zhang, C.; Li, X.; Hu, J. High Performance of Hot-Carrier Generation, Transport and Injection in TiN/TiO_2 Junction. *Front. Phys.* **2022**, *17* (5), 53509. https://doi.org/10.1007/s11467-022-1171-4.
(45) Xu, X.; Dutta, A.; Khurgin, J.; Wei, A.; Shalaev, V. M.; Boltasseva, A. TiN@TiO_2 Core–Shell Nanoparticles as Plasmon-Enhanced Photosensitizers: The Role of Hot Electron Injection. *Laser Photonics Rev.* **2020**, *14* (5), 1900376. https://doi.org/10.1002/lpor.201900376.
(46) Deka, T.; G Nair, R. Recent Advancements in Surface Plasmon Resonance and Schottky Junction Assisted Photocatalytic Water Splitting of Noble Metal Decorated Titania: A Review. *Int. J. Hydrogen Energy* **2024**, *59*, 322–342. https://doi.org/10.1016/j.ijhydene.2024.02.002.
(47) Singh, R.; Sial, Q. A.; Kim, U.; Nah, S.; Seo, H. Ultrafast Hot-Electron Injection at HfN-Metal Oxide Heterojunctions: Role of Barrier Height. *Mater. Sci. Semicond. Process.* **2022**, *152*, 107117. https://doi.org/10.1016/j.mssp.2022.107117.
(48) Baffou, G.; Bordacchini, I.; Baldi, A.; Quidant, R. Simple Experimental Procedures to Distinguish Photothermal from Hot-Carrier Processes in Plasmonics. *Light Sci. Appl.* **2020**, *9* (1), 108. https://doi.org/10.1038/s41377-020-00345-0.
(49) O'Neill, D. B.; Frehan, S. K.; Zhu, K.; Zoethout, E.; Mul, G.; Garnett, E. C.; Huijser, A.; Askes, S. H. C. Ultrafast Photoinduced Heat Generation by Plasmonic HfN Nanoparticles. *Adv. Opt. Mater.* **2021**, *9* (19), 2100510. https://doi.org/10.1002/adom.202100510.
(50) Verma, R.; Sharma, G.; Polshettiwar, V. The Paradox of Thermal vs. Non-Thermal Effects in Plasmonic Photocatalysis. *Nat. Commun.* **2024**, *15* (1), 7974. https://doi.org/10.1038/s41467-024-51916-3.
(51) Wang, D.; Zhou, Z.-H.; Yang, H.; Shen, K.-B.; Huang, Y.; Shen, S. Preparation of TiO_2 Loaded with Crystalline Nano Ag by a One-Step Low-Temperature Hydrothermal Method. *J. Mater. Chem.* **2012**, *22* (32), 16306–16311. https://doi.org/10.1039/C2JM16217B.
(52) Zhang, Q.; Lima, D. Q.; Lee, I.; Zaera, F.; Chi, M.; Yin, Y. A Highly Active Titanium Dioxide Based Visible-Light Photocatalyst with Nonmetal Doping and Plasmonic Metal Decoration. *Angew. Chem. Int. Ed.* **2011**, *50* (31), 7088–7092. https://doi.org/10.1002/anie.201101969.
(53) She, P.; Xu, K.; He, Q.; Zeng, S.; Sun, H.; Liu, Z. Controlled Preparation and Visible Light Photocatalytic Activities of Corn Cob-like Au–ZnO Nanorods. *J. Mater. Sci.* **2017**, *52* (6), 3478–3489. https://doi.org/10.1007/s10853-016-0639-4.
(54) Schneider, C. A.; Rasband, W. S.; Eliceiri, K. W. NIH Image to ImageJ: 25 Years of Image Analysis. *Nat. Methods* **2012**, *9* (7), 671–675. https://doi.org/10.1038/nmeth.2089.